Emergent quasi-two-dimensional electron gas between $Li_{1\pm x}NbO_3$ and $LaAlO_3$ and its prospectively switchable magnetism

I. V. Maznichenko [1,2,*] S. Ostanin,[1] I. Mertig,[1] and P. Buczek [2]

[1]*Institute of Physics, Martin Luther University Halle-Wittenberg, D-06099 Halle, Germany*
[2]*Department of Engineering and Computer Sciences, Hamburg University of Applied Sciences, Berliner Tor 7, D-20099 Hamburg, Germany*

Oxide interfaces between insulating perovskites can provide a two-dimensional electron gas (2DEG), which was observed initially beneath polar LaAlO₃ (LAO) grown on TiO₂-terminated SrTiO₃(001). Here, we suggest to use a solid electrolyte LiNbO₃ (LiNO) instead of SrTiO₃ to create in LAO/LiNO a robustly switchable and magnetic quasi 2DEG (q2DEG). This prospective phenomenon is achieved by charging and discharging lithium niobate while its $n \rightarrow p$ doping induces the alteration of magnetic order in LAO/LiNO and, thus, the spin degrees of freedom in q2DEG. On the basis of *ab initio* calculations and starting from the defectless and insulating LAO/LiNO superlattice, we demonstrate that either a ferromagnetic q2DEG or weakly magnetic quasi-2D hole gas emerge there due to the presence of excessive electrons or holes, respectively. These defects were simulated by one extra Li and a lithium vacancy in LiNO. By varying the LiNbO₃ thicknesses up to 18 formula units, we found that (i) the spatial extent of q2DEG is 1.5 nm along the stacking direction and that (ii) the dopant position at the Al-terminated interface is energetically preferable by more than 0.5 eV compared to the deep layers. In the context of the advanced design of q2DEG, the out-of-plane electric polarization, which intrinsically appears in multiferroic LAO/LiNO, allows to switch externally the electric-field dependence of the Rashba effect. Moreover, the in-plane charge current via q2DEG may generate there a transverse spin density due to the Rashba-Edelstein effect. We discuss this scenario using the relativistic electronic structures and locally projected density of states which differ remarkably in LAO/Li₁₊ₓNO and LAO/Li₁₋ₓNO.

I. INTRODUCTION

In 2004, a two-dimensional electron gas (2DEG) was observed between insulating perovskites LaAlO₃ (LAO) and SrTiO₃(001) (STO) [1–3]. Currently, the nature of this 2DEG is well understood [4–7]. At least, one of these two perovskites has to be polar, such as LAO(001) and, therefore, each La at the LaO/TiO₂-terminated interface transfers half of an electron into the next TiO₂ layer that decreases the oxidation state of interfacial Ti [8–11]. Thus, the low conduction band, which is formed by the Ti d-states, crosses the Fermi level and reveals 2DEG. Its extremely high mobility of up to 10^4 cm²/Vs is realized by a ionic-liquid-assisted field effect [12].

Regarding intrinsically imperfect interfaces, the variation of vacancies and intermixed cations simulated from first principles displays how the 2DEG density can be tuned externally. Oxygen vacancies, for instance, enhance 2DEG [13], while both the La/Sr mixing [14] and the cation vacancies suppress it [15,16]. So far, however, a limited number of experiments focused on the tuning of 2DEG [17,18], whereas liquid gating may allow to do that by controlling depletion of charged carriers. Electrolyte gating is commonly used for accumulating large carrier densities at the oxide surfaces [19]. With the change of gate voltage and polarity, the 2DEG's conductivity can be varied from its large value down to zero. This is under-

stood in terms of oxygen migration. By choosing the proper gate geometry and polarity, some of the intrinsic oxygen vacancies in LAO and those accommodated at the interface, can be filled. Then, by switching the gate polarity the O^{2-} ions can be partially pulled out that makes the composition of LAO/STO oxygen-deficient. Although the switching is not completely reproducible, it allows to explore the effect of electrolytic gating on 2DEG of LAO/STO through measurements of electrical transport, x-ray absorption spectroscopy, and photoluminescence spectra [12,20–24]. The controlled formation of 2DEG via ionic liquid gating has been shown recently for the LaFeO₃/STO interface [25].

Here, we suggest to use hexagonal lithium niobate, a solid-state electrolyte, instead of STO and ionic liquid gating. The unit cell of LiNbO₃ (LiNO) contains six formula units (f.u.), while their stacking sequence of cations in the octahedral sites, such as Nb/Li/vacancy and so on, makes LiNO the polar material. Since the 1960s thin LiNO films were used in many multifunctional devices, which utilize the ferroelectric (FE) properties of this material (nonvolatile memory, electrooptical modulation, FE sensitivity) and the surface acoustic wave devices [26]. Besides, thin LiNO films can be the basis for creation of perspective types of random-access memories, namely, FE-RAM and resistive RAM. We believe that the use of electrolytic and ferroelectric LiNO opens an opportunity for externally controlled 2DEG.

The LiNO geometry forces the LAO overlayer to be polar. In the (111)-ordered ABO_3 perovskite, the layer stacking is

---

*igor.maznichenko@physik.uni-halle.de

AO_3/B, with the charge mismatch of $0.5e$ and reduced trigonal symmetry, which lifts the degeneracy of the t_{2g} states into e_g and a_{1g}. In LAO/STO(111), its 2DEG has been observed recently [27–30] whereas the effect simulated for the perfect interface from first principles [15] is relatively weak. In the scenario of LAO/LiNO, the broken inversion symmetry lifts the spectral degeneracy of 2DEG. This is known as the Rashba spin-orbit coupling (SOC) effect [31]. The properties of LiNO allow, in principle, to extend the ordinary electric-field dependence of Rashba SOC [32,33] to its switching option. The Rashba SOC can be realized, for instance, by the polarization reversal in ferroelectric LiNO that may accumulate or deplete interfacial charged carriers. Recently, a spin-orbitronic concept of the FE-controlled spin-charge conversion has been suggested by Noël *et al.* [34]. The authors demonstrated how a nonmagnetic Rashba system efficiently generated spin current due to the Rashba-Edelstein effect [35]. The breaking of inversion symmetry at the interface resulted in the out-of-plane electric field. Then, the in-plane charge current via interfacial 2DEG produced a transverse spin density, which can diffuse as a spin current into the adjacent material [36].

Another mechanism of tunable 2DEG in LAO/LiNO may be realized by utilizing ionic transport. The shortage of Li during the growing of LiNO is a predominant source of ionic disorder. Thus, the thermally activated hopping or tunneling must go in the material. In this work, we mimic the discharged and charged LiNO side of LAO/LiNO by one Li vacancy (V_{Li}) and by one extra Li, respectively. Each point defect was relaxed at its preferable positions near the interface. This choice was motivated by the contact-limited conduction mechanism, which should dominate in the LiNO-based heterostructures. Focusing on the electronic structure of LAO/LiNO, LAO/Li$_{1-x}$NO, and LAO/Li$_{1+x}$NO ($x \approx 0.17$), we explore the Rashba SOC effect on 2DEG and also the 2DEG's magnetism, which is induced by defects in this formally nonmagnetic oxide system.

The magnetism of LAO/STO(001) was reported shortly after the discovery of 2DEG [37]. Until recently, its explanations used exclusively the mechanism of oxygen vacancies and Ti^{3+} at the interface [38,39]. The emergence of ferromagnetism in the Al-deficient LAO/STO was observed recently by Park *et al.* [40], who proposed the mechanism based on the cation vacancies. In this context, both the Li vacancy and Li impurity placed at the vacant cation site of LiNO may induce highly desirable magnetic q2DEG in LAO/LiNO. Moreover, by changing the Li content around nominally neutral composition of LiNO, one can switch the magnetic property of q2DEG from the ferromagnetically interacting moments induced on Nb species to weakly a magnetic solution, where its spin polarization is distributed between oxygens of LAO.

II. DETAILS OF *AB INITIO* CALCULATIONS

The electronic properties and structural optimization of the stoichiometric LAO/LiNO, Li-deficient LAO/Li$_{1-x}$NO and Li-excessive LAO/Li$_{1+x}$NO were computed using the Vienna *Ab initio* Simulation Package (VASP) [41], within the Perdew-Burke-Ernzerhof generalized-gradient approximation (GGA) [42] to the exchange-correlation potential. For bulk LiNbO$_3$, the use of this GGA yields the equilibrium volume,

which underestimates its experimental value insignificantly by <0.5%. Thus, in all simulations of hexagonal LAO/LiNO, the in-plane lattice parameter of LiNO, $a = 5.223$ Å, is used that may well mimic the growth conditions of the interface at its lattice mismatch. The electron-ion interactions were described by projector-augmented wave pseudopotentials and the electronic wave functions were represented by plane waves with a cutoff energy of 450 eV. Regarding the PAW potentials, the valence configurations $3s^2 3p^1$, $2s^2 2p^4$, and $2s^1 2p^0$ are used for Al, O, and Li, respectively. The pseudopotential for La is in the $5s^2 5p^6 5d^1 6s^2$ configuration, in which the 5s5p semicore states are treated as valence states. The Nb pseudopotential is in the $4p^6 5s^2 4d^3$ valence configuration which includes the semicore $4p$ states.

It was established that perovskites grow in complete unit cells [43,44]. Thus, we constructed the LAO/LiNO superlattices starting from the 6-f.u.-thick LiNO (0001) and 6-f.u.-thick LAO (111). Here, the LAO side exceeds its known critical thickness of four unit cells needed to form the 2DEG in LAO/STO. Then, we increased the LAO thickness to 12 f.u. and varied the thicknesses of LiNO ranging between 6 f.u. and 18 f.u. that allows to localize the extent of q2DEG. The experimental lattice parameters of bulk LiNO were used for the in-plane geometry of LAO. There were two chemically different terminations of LAO in LAO/LiNO, namely, (i) LaO$_3$ and (ii) Al, while the interfacial LiNO layer contained, respectively, the cations and O, which formed structurally the BO$_6$ octahedra similar to those of bulk material. The two interfaces differed from each other due to the presence or absence of La between octahedra. Ionic relaxation of the whole supercell was performed using the conjugate-gradient algorithm until the Hellmann-Feynman forces became less than 1×10^{-2} eV/Å. The use of the $6 \times 6 \times 2$ **k**-mesh yielded the reliable atomic positions. The 6-f.u./6-f.u.-thick LAO/LiNO supercell after relaxation is shown in Fig. 1. The density of states (DOS) was obtained using the tetrahedron method on the Γ-centered $8 \times 8 \times 3$ **k**-mesh. The DOS and band structure calculations were performed in the presence of SOC [45].

III. RESULTS AND DISCUSSION

A. Perfect LAO/LiNO

Ab initio calculations, within the GGA, give for bulk LiNO and hexagonal LAO the band-gap values of 3.33 eV and 2.7 eV, respectively. The insulating gap computed for the LiNO heterostructure tends to diminish. These trends have been recently demonstrated by Gao *et al.* [46] for all-solid-state battery with LiNO electrolyte. In this work, stoichiometrically perfect LAO/LiNO was simulated by the 60-atom superlattice constructed from $6 + 6$ f.u. stacked along the z-axis. The energy positions of the valence band maximum and the conduction band minimum, which are plotted in Fig. 2 for each atomic layer after relaxation, show an insulating band-edge profile that is surprising since the both materials are polar in this geometry.

Apart from a polar discontinuity the potential step between LiNO and LAO forms band bending. It seems that the band bending in LAO/LiNO after relaxation is not so strong, as compared to LAO/STO. In LAO/STO, with decreasing the
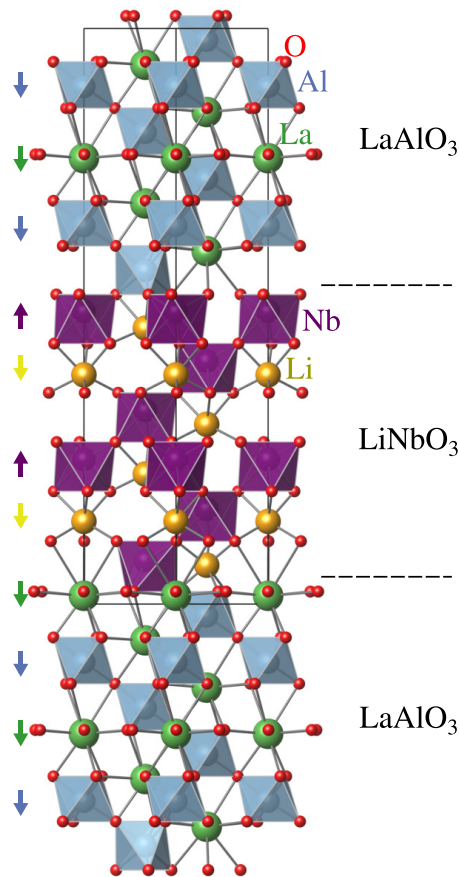
FIG. 1. Atomic structure of $LaAlO_3$/$LiNbO_3$. La atoms are shown in green, Al in blue, Li in gold, Nb in magenta, and O atoms are shown in red. AlO_6 and NbO_6 octahedra are shown in blue and magenta, respectively. The rectangular box labels the 60-atom super-cell used to simulate the 6-u.c./6-u.c.-thick LiNO/LAO superlattice. The intralayer displacements of oxygens and cations induced in LAO and the cation displacements from the center of O_6 octahedron are marked by arrows.
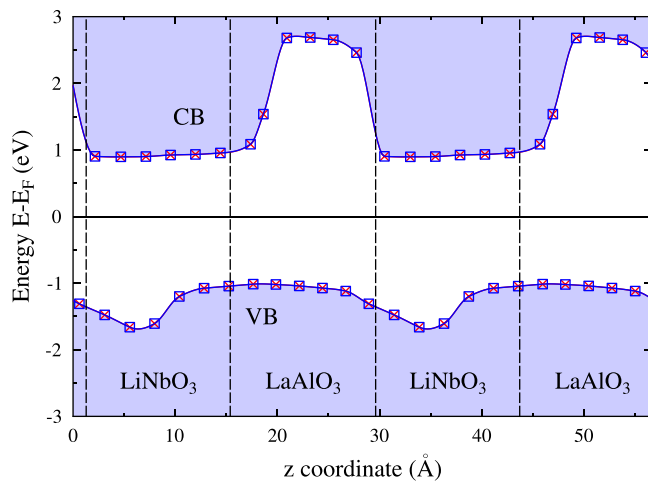

FIG. 2. The layer-resolved band profile of stoichiometric $LaAlO_3$/$LiNbO_3$, plotted vs the layer position along z-direction. Both the insulating band character and zero spin polarization are shown.
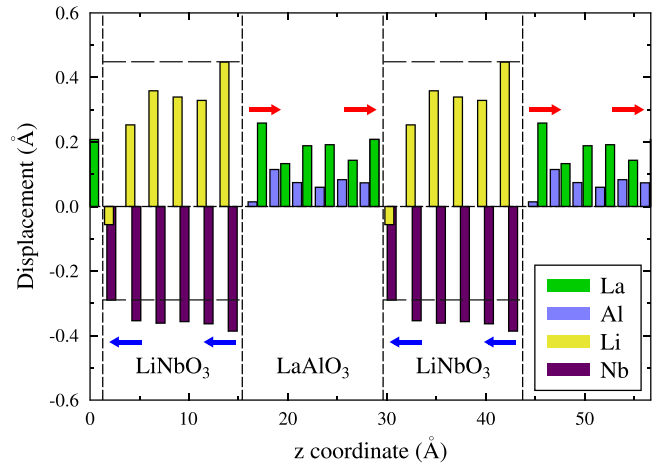

FIG. 3. The cation displacements d_z calculated in $LaAlO_3$/$LiNbO_3$ along z-direction after relaxation. For Al, Li, and Nb, their d_z, shown in blue, gold, and magenta, respectively, are the cation displacements from the center of O_6 octahedron plotted in Fig. 1. For each La, the calculated intralayer displacement, $d_z = z_{La} - z_O$, is shown in green. The d_z values of Li and Nb in bulk $LiNbO_3$ are indicated by dotted lines for comparison. The electric polarization direction in LiNO as well as the polarization induced in LAO are marked by arrows.

LAO thickness the band bending increases. For instance, the band-edge profile of the 2-f.u.-thick LAO resembles that of typically ferroelectric material [15]. Obviously the use of ultrathin LAO in LAO/LiNO may induce 2DEG there. On the other hand, bulk LiNO is ferroelectric. The effect of 2DEG between STO and a robust ferroelectric was recently anticipated from first principles [47,48]. In LAO/LiNO, its LiNO side might promote the q2DEG. However, according to our simulations, the effect does not appear there. This result needs further detalization of the crystal structure related to spontaneous electric polarization of LiNO.

The displacements of each cation of $LaAlO_3$/$LiNbO_3$, d_z, are plotted in Fig. 3. This gives an idea of the magnitude of electric dipols and how these dipols vary toward the interfaces. For Al, Li, and Nb, their d_z's were obtained as the displacements from the center of O_6 octahedron. For La, its d_z is the intralayer displacement, $d_z = z_{La} - z_O$. For Li and Nb in LiNO, their displacements are opposite to each other. The Li d_z's decrease gradually from its bulk value of 0.45 Å seen near the Al-terminated interface to marginally negative -0.05 Å at the LaO_3-terminated interface. Contrary, the Nb displacements increase from the bulk magnitude of -0.29 Å near the LaO_3 interface to about -0.4 Å obtained at the Al-terminated interface of LAO/LiNO. Thus, negative Nb–O dipols dominate in LiNO layers over positive O–Li dipols that forces electric polarization to be directed toward the Al-terminated interface. In contrast, in bulk LAO, all atomic displacements along [111] are zero. Interestingly, for LAO/LiNO we see in Fig. 3 that all cations are displaced positively. The Al displacements vary below 0.1 Å while d_z of La vary around 0.2 Å that should induce in LAO electric polarization directed towards the Al-terminated interface. It seems that this induced polarization in LAO is a key factor which prevents the heterostructure from the q2DEG.
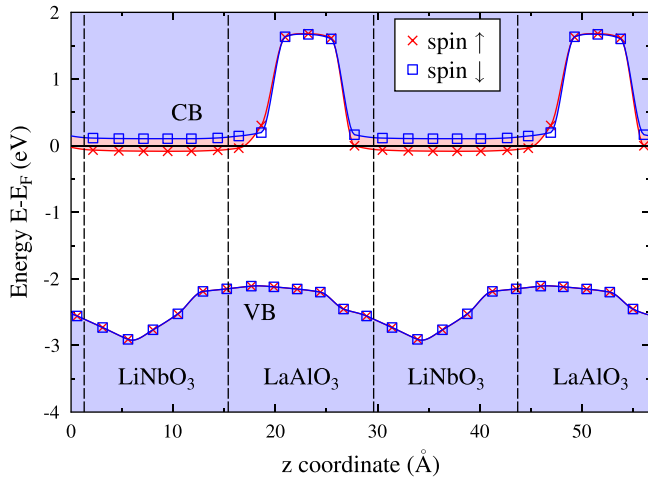
FIG. 4. The spin-polarized band profile of LaAlO$_3$/Li$_{1+x}$NbO$_3$ ($x = 0.17$) plotted vs the layer position along z-direction.

B. Li-excessive LAO/Li$_{1+x}$NO

When one lithium is added to the 60-atom supercell of LAO/LiNO this allows to simulate the n-doped LAO/Li$_{1.17}$NO. There are several options to place the Li dopant in LiNO. The dopant position, however, does not affect critically the electronic structure of LAO/Li$_{1.17}$NO. For that reason we focus below on the lowest-energy case where an extra Li is placed in the cation vacancy position near the Al-terminated interface. As Fig. 4 shows, the profile of the band edges in LAO/Li$_{1.17}$NO changes qualitatively as compared to the defectless LAO/LiNO. Most importantly, the q2DEG appears now. One can see, therefore, that the n-doped LiNO displays its entirely conducting layers and interfaces, which are separated by insulating LAO along the stacking direction.

The Li-excessive LAO/Li$_{1+x}$NO resembles the scenario of oxygen vacancies at the (001) LAO/STO interface. First, interfacial oxygen vacancies yield n-doped LAO/STO and notably enhance its 2DEG. Second, oxygen vacancies reduce the oxidation state of nearest Ti from 4+ to 3+ inducing, therefore, the magnetic moment on these species. In LAO/STO, the coexistence of ferromagnetism and enhanced 2DEG was simulated [38] from first principles, within the Hubbard parametrization on the 3d-states of interfacial Ti. For LAO/Li$_{1+x}$NO, we show that q2DEG and ferromagnetic order coexist in the frameworks of conventional GGA.

The total spin-polarized density of states (DOS) of LAO/Li$_{1.17}$NO is shown in Figures 5(a) to 5(b). The most important DOS features are seen there near the conduction band edge. The lowest spin-majority band is occupied so that its bottom is about 70 meV below the Fermi level (E_F). Since the ferromagnetic exchange shifts the spin-minority conduction band by 0.1 eV above E_F, the q2DEG in LAO/Li$_{1+x}$NO appears to be purely half metallic, as Fig. 5(b) shows. The integral DOS seen in Fig. 5(c) visualizes the spin-polarization of n doping. Figure 5(d) illustrates that total magnetization of LAO/LiNO with one extra Li is ~ 1 μ_B. The use of the rigid band model suggests that the 1-μ_B-magnetization may change insignificantly with increasing chemical potential up to $E_F + 0.03$ eV. This is because the total magnetization of
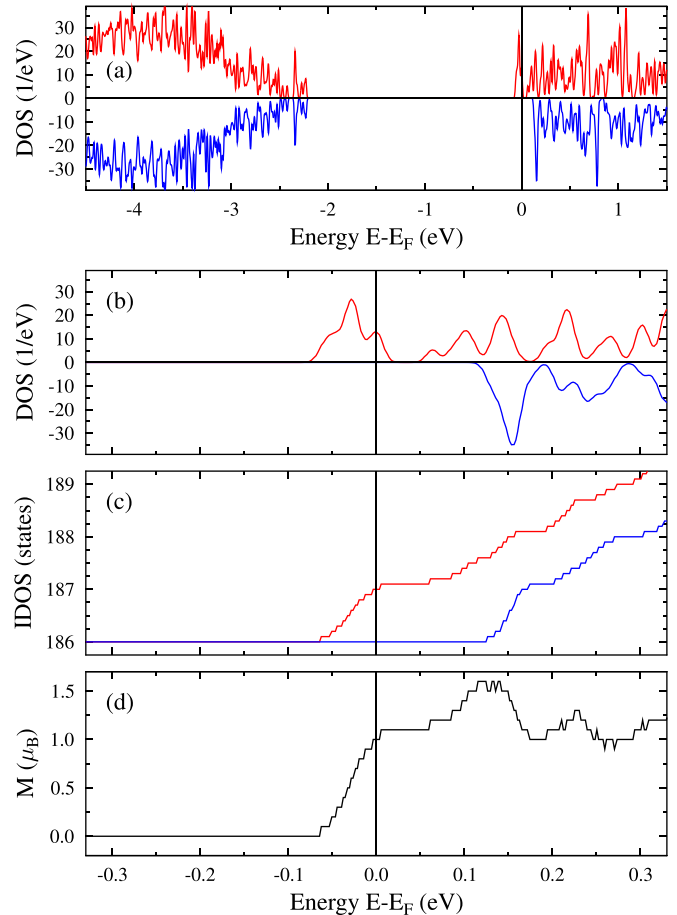

FIG. 5. The (a) total spin-polarized DOS, (b) its details near E_F, (c) the integral DOS, and (d) total magnetization calculated for LaAlO$_3$/Li$_{1.17}$NbO$_3$.

1 μ_B is defined by n-doping with one electron. The magnetic properties were calculated here at zero temperature. Nevertheless, we believe that the ferromagnetism predicted for LaAlO$_3$/Li$_{1+x}$NbO$_3$ is robust since its ferromagnetic solution is strongly energetically preferable with respect to paramagnetic one.

In the low panel of Fig. 6, we plot the side view of the three-dimensional (3D) magnetization density of LAO/Li$_{1.17}$NO. The chosen isodensity value illustrates the spin $\uparrow$ character of induced magnetization on each Nb. All local magnetic moments induced in this formally nonmagnetic supercell are shown in top panel of Fig. 6. The dominating contributions to the total magnetization come from Nb species, the moments of which vary between 0.25 μ_B and 0.05 μ_B. The large values of m_{Nb} obey those 4d cations which are placed in the deep LiNO layers, whereas interfacial species show their $m_{Nb} \sim 0.05$ μ_B. The negative magnetic moments of oxygens in Li$_{1.17}$NbO are negligible, as well as those of all oxygens and cations in LAO. Hence, the total 1-μ_B-magnetization is distributed almost completely between six Nb. For the fixed amount of extra Li in the supercell, each value of m_{Nb} depends there on the LiNO thickness, i.e., simply on the number of 4d cations. The thicker Li$_{1+x}$NbO the smaller the m_{Nb} average.
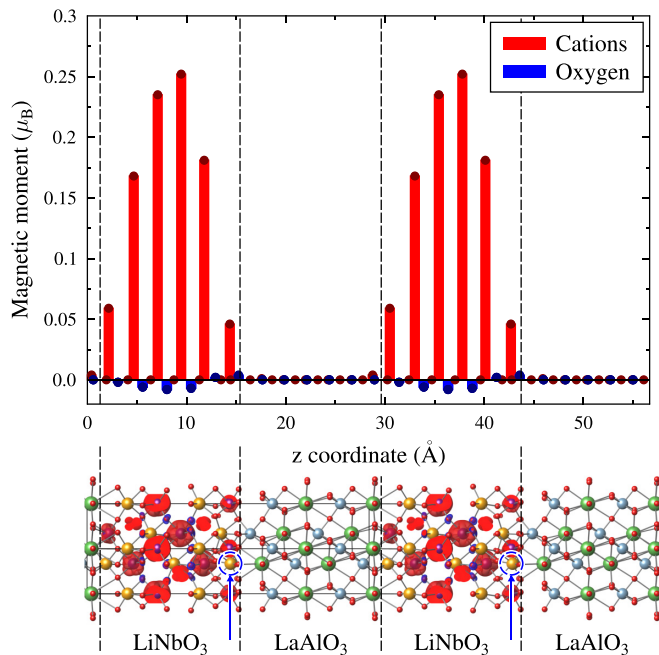
FIG. 6. The local magnetic moments induced in $LaAlO_3/Li_{1.17}NbO_3$ (top panel) and the side view of its magnetization density (low panel). To show the spin ↑ magnetization density (in red) induced on each Nb, the fixed isodensity value $\pm 0.001 \mu_B Å^{-3}$ was used. The position of an excessive Li near the interface is marked by blue arrow and circle.

Figure 7 shows the spin-projected band structures, calculated for $LaAlO_3/Li_{1.17}NbO_3$ and plotted along the two high-symmetry directions of the Brillouin zone. For each spin, this gives features of the electronic branches $E(k)$ and their population near E_F. The corresponding DOS is shown above in Fig. 5(b). One can see that q2DEG is formed there by the two spin ↑ branches. One of them, which is relatively flat, never crosses E_F, whereas the second parabolic branch
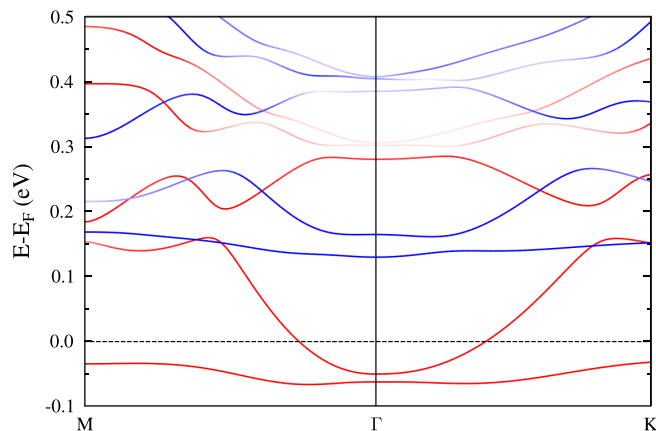

FIG. 7. The spin-projected band structure of $LaAlO_3/Li_{1.17}NbO_3$, plotted near E_F along the two high-symmetry directions of the Brillouin zone. The branches $E(k)$, in which the $4d$ states of a single interfacial Nb dominate, are plotted in red (spin ↑) and blue (spin ↓), while the color level indicates the $E(k)$ projection on Nb $4d$ states.
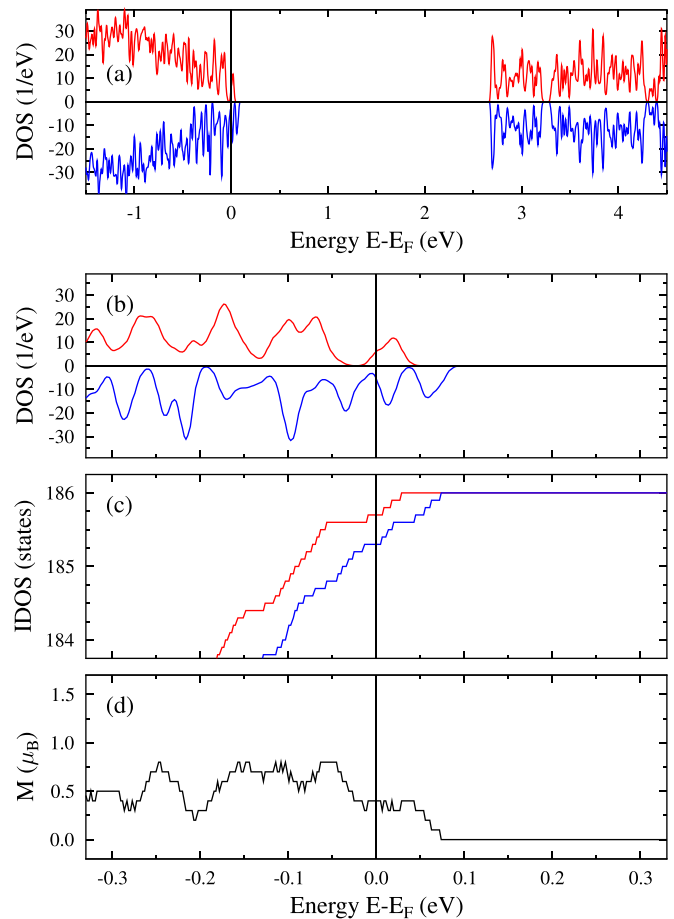

FIG. 8. The (a) total spin-polarized DOS, (b) its details near E_F, (c) the integral DOS, and (d) total magnetization of $LaAlO_3/Li_{0.83}NbO_3$.

crosses E_F from below around the Γ point, forming the Fermi surface cross section which is typical for q2DEG. The two low spin-minority branches of the conduction band of $LAO/Li_{1.17}NO$ appear both above E_F. We inspected also how these spin-projected low conduction bands are populated by the $4d$ states of a single interfacial Nb. This is depicted by red $E(k)$ in Fig. 7 where the population degree, which decreases from 0.17 to zero, is marked by changing the color level [49].

C. Li-deficient LAO/Li$_{1-x}$NO

To simulate the Li-deficient $LAO/Li_{1-x}NO$ which mimics this discharged material, we removed one Li from the supercell. Few options were inspected for the vacancy position. We focus below on the case where one Li was removed from the interface layer. The calculated DOS of $LAO/Li_{0.83}NO$, shown in Fig. 8, represents the typical picture of p doping. The top valence band moves up and forms a quasi-2D hole gas (q2DHG). In $LAO/Li_{1-x}NO$, this scenario of q2DHG repeats the physics of both the cation-deficient LAO/STO and AlO_2/SrO-terminated stoichiometric LAO/STO [15,40]. However, in $LAO/Li_{0.83}NO$ its q2DHG appears simultaneously at the two terminations that differs it from the LAO/STO superlattice.
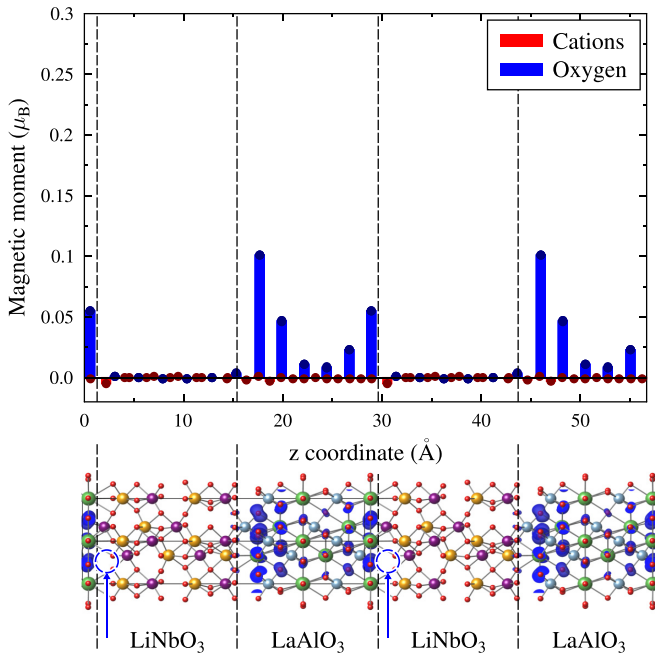
FIG. 9. The local magnetic moments induced in $LaAlO_3/Li_{0.83}NbO_3$ by a single Li vacancy (top panel) and the side view of the corresponding magnetization density (low panel). For the side view, its pronounced magnetization density, which is seen on oxygens in the LAO layers and which is marked by blue, was computed by fixing the isodensity value $\pm 0.001 \mu_B \mathring{A}^{-3}$. The first position of one removed Li near the interface is marked by blue circle.

The spin-polarized DOS of LAO/$Li_{0.83}$NO is plotted in Figs. 8(a) and 8(b). This shows how q2DHG is formed almost equally by the spin ↑ and spin ↓ electronic states, which extend above E_F up to 0.05 eV and 0.1 eV, respectively. For the one-Li-vacancy LAO/$Li_{0.83}$NO, its integral spin-projected DOS and magnetization, plotted in Figs. 8(c) and 8(d), suggest that the magnetization value may decrease from ∼0.5 μ_B at E_F to zero for $E > E_F + 0.1$ eV.

The side view of the magnetization density in $LaAlO_3/Li_{0.83}NbO_3$ is plotted in Fig. 9 (low panel). By choosing the suitable isodensity value, we identify all magnetic moments induced in this supercell. Interestingly, the notable moments induced there belong to oxygens located in the LAO side only. In the top panel of Fig. 9, we show the magnetic moments accumulated in each layer of LAO/$Li_{0.83}$NO. It should be noted that each oxygen-rich layer of the supercell contains three O. Accordingly, their relatively large individual contributions up to 0.1 μ_B to the total magnetization of 0.5 μ_B comes from the interfacial layers of LAO, while its deeper O_3 layers contribute much less. All O species in the $Li_{0.83}$NO layers are nonmagnetic. In LAO/Li_{1-x}NO, thus, the number of notably magnetic species, with their moments of ∼0.1 μ_B per each O, is extremely small, as compared to the total O amount. Usually, such weak magnetism in the buried interfaces is difficult to measure. For example, the use of x-ray magnetic circular dichroism (XMCD) can be inappropriate for the Li-deficient LAO/LiNO because of its marginal dichroic signal. Instead,
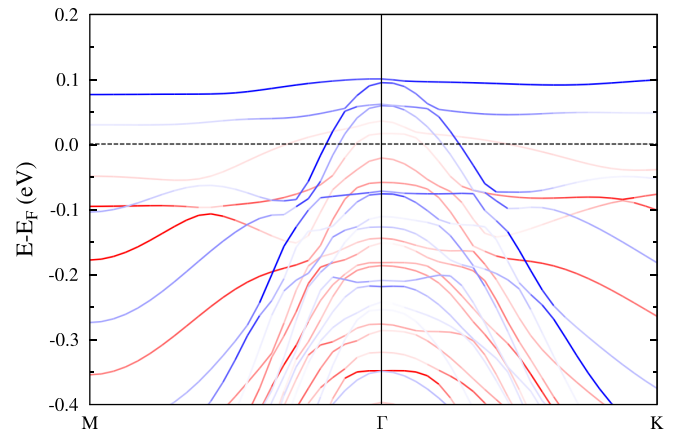

FIG. 10. The spin-projected band structure of $LaAlO_3/Li_{0.83}NbO_3$, which is plotted near E_F. The electronic branches populated by the spin-polarized p states of one interfacial O are shown in red (spin ↑) and blue (spin ↓), while the color level indicates the $E(k)$ projection on O p states.

the magnetoelectric properties of this q2DHG interfaces can be studied using magnetotransport measurements [40].

In Fig. 10, the spin-projected $E(k)$ of the upper valence band of LAO/$Li_{0.83}$NO are plotted along the $k_z = 0$ directions. For the spin-majority valence band, there are two branches seen along each high-symmetry direction, which cross E_F from below around Γ-point and which both are marginally populated by the spin ↑ p states of interfacial oxygen. The spin-minority band structure is more complicated. Besides the two upper branches, which cross E_F similarly to those of the opposite spin, there is a pair of branches, which appear above E_F and which may show relatively low effective mass. Concerning the second pair, only one of these branches is populated by the spin ↓ p states of interfacial O, which was selected for this presentation. To gain further insight into the band structure of defective LAO/LiNO the SOC effect needs to be included, within the *ab initio* calculations.

D. Effect of the spin-orbit coupling

Figure 11 shows how the q2DEG band structure of LAO/$Li_{1.17}$NO changes when the spin polarization, SOC, and spin degree beyond collinearity are allowed step by step. First,

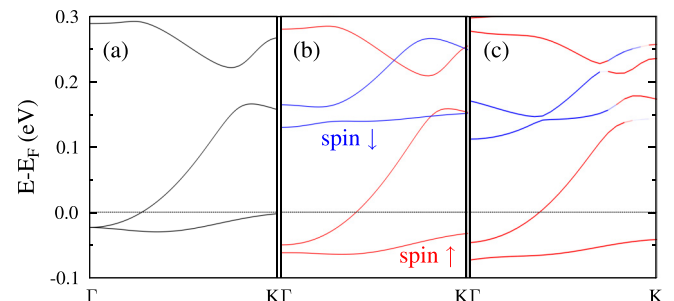FIG. 11. The q2DEG band structure of $LaAlO_3/Li_{1.17}NbO_3$ along Γ – K, which was calculated using the (a) non-spin-polarized and (b) spin-polarized nonrelativistic modes, and also using both the SOC and (c) noncollinear degrees of freedom.
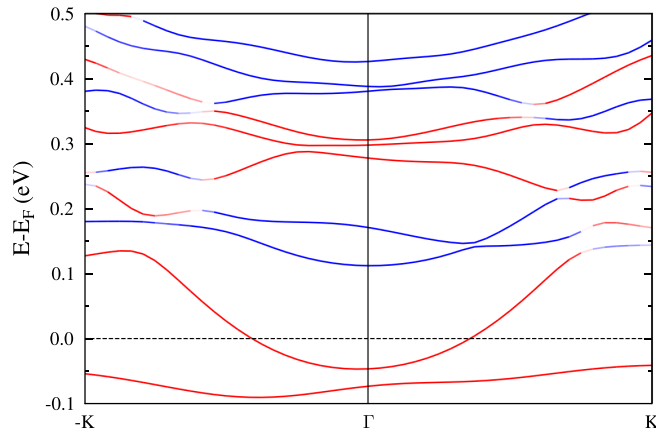
FIG. 12. The relativistic and noncollinear band structure of q2DEG in LaAlO$_3$/Li$_{1.17}$NbO$_3$, plotted near E_F along the $-$K – Γ – K directions of the Brillouin zone.

FIG. 13. The relativistic and noncollinear band structure of q2DHG in LaAlO$_3$/Li$_{0.83}$NbO$_3$, which is plotted near E_F along $-$K – Γ – K.

the magnetic exchange extends the location of q2DEG that is seen in Fig. 11(b). The Fermi surface topology, however, is not changed qualitatively by the spin polarization allowed. Here, the expected degeneracy lifting takes place above E_F, between $E_F + 0.15$ eV and $E_F + 0.3$ eV, where the two spin $\downarrow$ branches appear. Finally, the SOC and spin noncollinearity, which were allowed simultaneously, mix the spin states and remove all previous band crossings. Indeed, this is seen in Fig. 11(c). It should be noted that after relaxation the supercell symmetry was reduced to primitive in all calculations presented in Fig. 11.

The effect of noncollinearity needs further consideration. In Fig. 12, the noncollinear relativistic band structure of LAO/Li$_{1.17}$NO is plotted along its two formally identical directions $-$K – Γ and K – Γ. The asymmetry seen there appears due to the notable in-plane component of induced magnetization. The issue of induced asymmetry in the band structure is widely discussed in the literature in the context of SOC (see, for instance, the recent paper by Tao and Tsymbal and references therein [50]). The interfacial Rashba SOC effect is a momentum-dependent spin splitting of $E(\mathbf{k})$ which occurs in LAO/LiNO due to its broken space-inversion symmetry. However, when the interface is doped by extra Li the SOC-affected system can also show a Zeeman effect, i.e., the momentum-independent spin splitting of the energy bands. The internal exchange field, arising in Li$_{1.17}$NbO$_3$ from its induced magnetization produces a nonnegligible Zeeman splitting of $E(\mathbf{k})$. One can expect that the interplay between the Rashba and Zeeman effects may lead to some specific features of $E(\mathbf{k})$. For instance, the band asymmetry seen in Fig. 12 is the result of the combined Rashba-Zeeman effect. In LAO/Li$_{1.17}$NO for the energy branches crossing E_F, we evaluate the momentum shift $\Delta q = 0.028 \text{Å}^{-1}$. For comparison, in trigonal layered PtBi$_2$ the reported momentum offset [51] is 0.045 Å^{-1}. It should be noted that broken time-reversal symmetry caused by the in-plane exchange field may give rise to the anomalous Hall effect in the LAO/Li$_{1.17}$NO system.

In LAO/Li$_{0.83}$NO, the geometry of heterostructure forces relatively weak magnetization to lie in the x-y plane. As the result, the band structure of q2DHG, which is plotted in
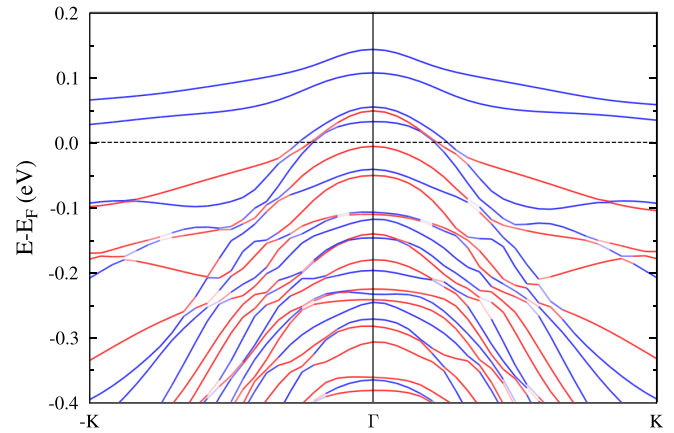
Fig. 13, seems modestly asymmetric that indicates the minor Zeeman contributions to the total band splittings associated with q2DHG. One can suppose, therefore, that the energy band asymmetry should not affect the transport properties of undoped LAO/Li$_{0.83}$NO.

We found, thus, that the in-plane oriented magnetization of LAO/Li$_{1\pm x}$NO induces the band asymmetry while the SOC changes the q2DEG/q2DHG bands effectively when bias voltage of 150 mV is applied. In this interface, the SOC yields the picture which differs critically from that of the "classically" splitted parabolic q2DEG bands of cubic LAO/STO. In the low-symmetry interface LAO/Li$_{1\pm x}$NO, its magnetic exchange emerges similar band splittings before the SOC is switched on.

E. Spatial extent of q2DEG and q2DHG

In LAO/Li$_{1.17}$NO, the induced electron density covers entirely the 6-f.u.-thick layer of LiNO, while the increase of the LAO thickness from 6 f.u. to 12 f.u. does not change the picture. To study the spatial extent of q2DEG along the stacking direction of the Li-doped LAO/LiNO, we calculated the 12-f.u.-thick and 18-f.u.-thick LiNO. For each of these three thicknesses of LiNbO$_3$, we plot in Fig. 14 their layer-resolved DOS values, $n(E_F)$, calculated at the Fermi energy along the stacking direction. All three relaxed superlattices contain six f.u. of LAO and one extra Li placed at the Al-terminated interface. For the 6-f.u.-thick LiNO, the electron density covers entirely the layer of LiNO showing the maximal value in the middle of doped LiNO. With increasing the thickness of LiNO to 12 f.u., the electron density transforms into the double peak profile with a deep minimum between two peaks in the middle of doped LiNO. The 18-f.u.-thick LiNO shows distinctly the two electron density peaks separated by insulating layer of about 1 nm in the middle of LiNO. The magnitudes of the two peaks of $n(E_F)$ are not equal to each other. The electron density seen near the dopant position at the Al-terminated interface is significantly larger than that induced near the chemically perfect LaO$_3$-terminated interface, while each peak density extends spatially by the same 1.5 nm. Thus, when the thickness of LiNO in n-doped LAO/LiNO
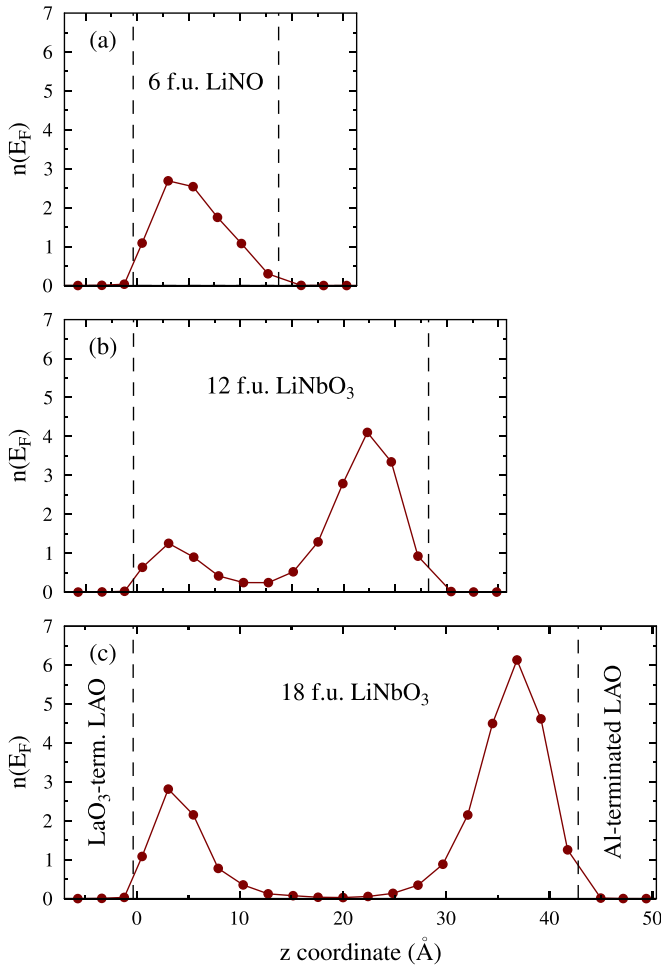
FIG. 14. The layer-resolved density of states at $E = E_F$ in Li-doped LAO/LiNO calculated along the stacking direction for the (a) 6-f.u.-thick, (b) 12-f.u.-thick, and (c) 18-f.u.-thick LiNO. For each superlattice, the layer positions start from the LaO$_3$-terminated interface which is shown by dashed line.

exceeds 12 f.u., the quasi-2D electron density localizes within 1.5 nm beneath each interface. Figure 14(c) clearly illustrates the quasi-2D nature of the electron gas anticipated here. There are several examples in the literature when rather thick conducting layer of oxide interface ranging between 1.4 nm and 7 nm was reported as q2DEG [52,53]. Using the 6-f.u./18-f.u. superlattice of LAO/LiNO, we placed the Li dopant into the different vacant positions of LiNO. The corresponding relaxed energies are plotted in Fig. 15 versus the stacking direction. The dopant position at the Al-terminated interface is preferable by 0.5 eV and by 2.6 eV compared to those when Li is placed in the middle of LiNbO$_3$ and at the La-terminated interface, respectively. In bulk LiNbO$_3$, all cation vacancies are energetically equivalent for the dopant. Figure 15 shows that the LAO side and its dually terminated interfaces play an important role for the q2DEG. The dopant position at the La-terminated interface is strongly unfavorable because of the nearest interfacial La which repels the dopant. However, the intrinsic electric polarization, which is directed toward the La-terminated interface in each of the two materials, prevents relaxation of these cations outward the interface. As for the
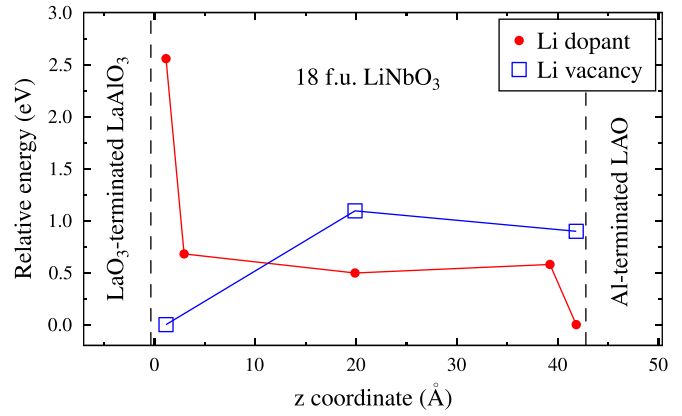

FIG. 15. Relative energetics of the n-doped (p-doped) LAO/LiNO, which are plotted vs vs the position of Li-dopant (Li-vacancy) along the stacking direction in the 18-f.u.-thick LiNO.

Li dopant placed at the Al-terminated interface, its position is supported environmentally and ferroelectrically.

For the case of the 6-f.u./18-f.u.-thick LAO/LiNO and by placing one Li consequently at each interface or in the middle of LiNO, we inspect how the dopant position affects both the

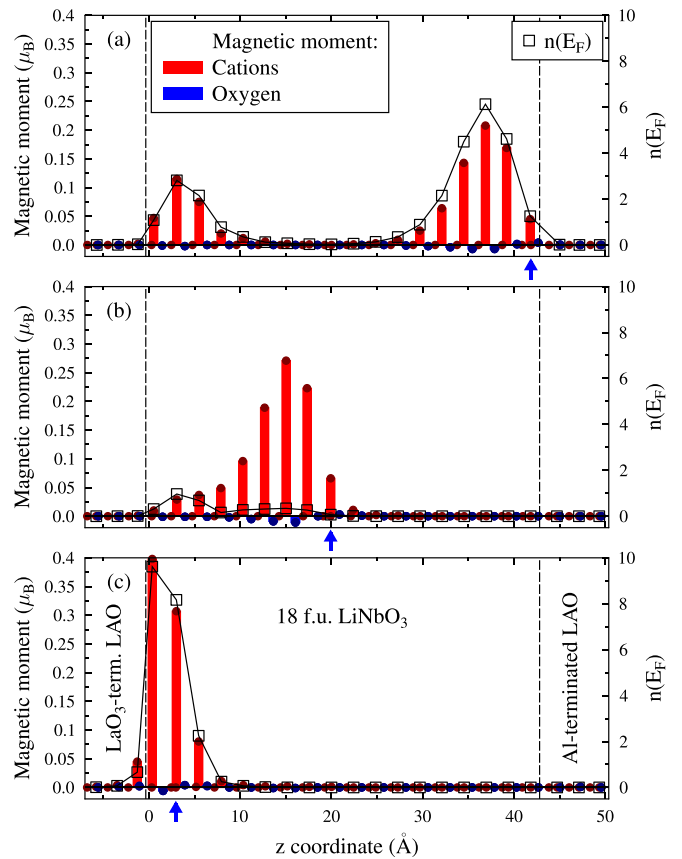FIG. 16. The site-projected magnetic moments on the cations (red) and oxygens (blue) as well as the layer-resolved density of states at $E = E_F$ (open box), which were calculated for the 6-f.u./18-f.u.-thick LAO/LiNO doped by one lithium. The position of dopant placed (a) at the Al-terminated interface or (b) in the middle of LiNO or (c) near the LaO$_3$-terminated interface is marked by blue arrow.
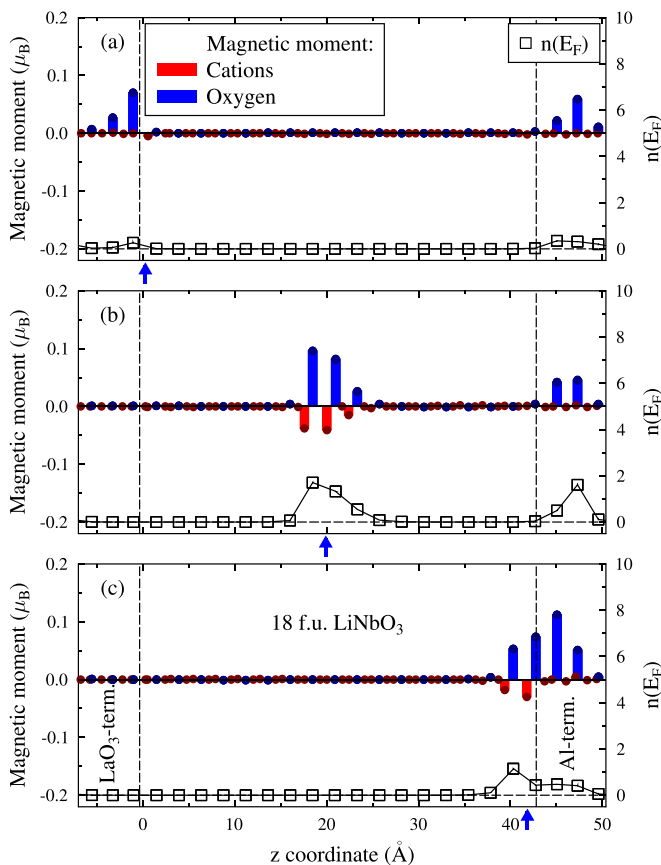
FIG. 17. The magnetic moments induced on the cations (red) and oxygens (blue) and the layer-resolved density of states at E_F (open box), which were calculated for the 6-f.u./18-f.u.-thick LAO/LiNO with one lithium vacancy. The V_{Li} position (a) at the LaO$_3$-terminated interface or (b) in the middle of LiNO or (c) at the Al-terminated interface is marked by blue arrow.

q2DEG and induced magnetism. In each of the three panels of Fig. 16, we plot the corresponding site-projected magnetic moments and the layer-resolved density of states at the Fermi level $n(E_F)$. When the dopant is placed in the most energetically preferable position at the Al-terminated interface, there is the second peak of q2DEG seen relatively far from the dopant and near the LaO$_3$-terminated interface. This picture is not changed with increasing the thickness of LAO up to 12 f.u.. In the n-doped LAO/LiNO superlattice, therefore, the electron transfer from the Al-terminated to the opposite interface occurs due to intrinsically ferroelectric LiNO. In particular, the main peak of q2DEG which, needs to be at the Al-terminated interface, is also shifted outward by several Å. The trend of shifted q2DEG toward the LaO$_3$ interface is seen in Fig. 16(b), which illustrates the simulated dopant position in the middle of LiNO. Finally, when the dopant appears near the LaO$_3$ interface, the further shift of q2DEG beyond LiNO is blocked by an electric field of LAO. In this scenario, the spatial extent of q2DEG does not exceed 1 nm while the magnetic moment induced on interfacial Nb may reach 0.4 μ_B.

As for V_{Li} in LAO/LiNO, its energy profile calculated along the stacking direction of the 18-f.u.-thick LiNO is plot-

ted in Fig. 15. The position of V_{Li} at the LaO$_3$-terminated interface is preferable by 1.1 eV and by 0.9 eV compared to those when V_{Li} is placed in the middle of LiNbO or at the Al-terminated interface, respectively. This is due to the electric polarization directed toward the LaO$_3$-terminated interface. In the static regime, thus, the Li vacancies tend to accommodate near the LaO$_3$-termination whereas the dopants may accommodate at the Al-terminated interface.

In Fig. 17, the layer-resolved density of states at E_F and the site-projected magnetic moments induced in the p-doped LAO/LiNO are plotted. For the energetically preferable vacancy position at the LaO$_3$-terminated interface, Fig. 17(a) shows that both the magnetic moments of marginal values and insignificant q2D hole density appear at the two interfaces simultaneously. When an extra Li vacancy is placed in the middle of the 18-f.u.-thick LiNO, as shown in Fig. 17(b), there are (i) the 1-nm-thick q2DHG around the defect and (ii) the minor q2DHG seen near the Al-terminated interface. The second of these is similar to the minor q2DHG emerging in Fig. 17(a). This secondary effect can be explained in terms of the rigid-band model. The upper point of the valence-band profile of stoichiometric LAO/LiNO which is shown in Fig. 2 corresponds to the Al-terminated interface. Obviously, in the p-doped system the valence band crosses E_F first there. As shown in Fig. 17(c), the presence of vacancy at the Al-terminated interface illustrates this scenario of q2DHG. Quantitatively, the q2DHG in doped LAO/LiNO can be about three times smaller than q2DEG of the same degree of doping.

IV. SUMMARY

Oxide interface between insulating LAO(111) and a solid-state electrolyte LiNbO$_3$ was modeled from first principles, within the superlattice where the thicknesses of each material were varied between 6 f.u. and 18 f.u.. We find that after relaxation the stoichiometric LAO/LiNO remains robustly insulating, whereas the q2DEG and q2DHG appear in the n- and p-doped heterostructures: LAO/Li$_{1+x}$NO and LAO/Li$_{1-x}$NO, respectively. The doping was simulated by adding or removing one lithium in the LiNO side.

For LAO/Li$_{1+x}$NO, we anticipate that its q2DEG is ferromagnetic and half-metallic. The total zero-K magnetization of 1 μ_B, which is induced there due to one extra Li, is distributed between Nb species. Most importantly, we predict fully spin-polarized q2DEG there. The dopant position at the Al-terminated interface is strongly preferable compared to those when Li is placed in the middle of LiNbO$_3$ and, especially, at the La-terminated interface. The electric polarization directed toward the La-terminated interface is responsible for that. For the most preferable dopant position in LAO/LiNO, its quasi-2D electron density localizes within 1.5 nm beneath each interface. A weakly magnetic 2D hole gas appears in the Li-deficient LAO/Li$_{1-x}$NO. We find there the 1-nm-thick q2DHG pinned to the vacancy position and rather small magnetic moments of $< 0.1 \mu_B$, which were induced mostly on oxygens. Although the LaO$_3$-terminated interface is strongly preferable for V_{Li}, the minor q2DHG always appears at the Al-terminated interface. Quantitatively, the q2DHG in doped LAO/LiNO is significantly smaller than q2DEG of the same degree of doping. These two conducting and presumably

magnetic 2D gases of doped LAO/LiNO may differ notably in their transport and magnetic properties. Thus, by charging and discharging the LiNO layers one can switch the magnetoelectric properties from q2DEG to q2DHG and vice versa. This scenario is a promising basis for spin-orbitronic devices and further implications.

[1] A. Ohtomo and H. Y. Hwang, Nature **427**, 423 (2004).

[2] S. Thiel, G. Hammerl, A. Schmehl, C. W. Schneider, and J. Mannhart, Science **313**, 1942 (2006).

[3] N. Nakagawa, H. Y. Hwang, and D. A. Muller, Nat. Mater. **5**, 204 (2006).

[4] H. Chen, A. Kolpak, and S. Ismail-Beigi, Phys. Rev. B **82**, 085430 (2010).

[5] H. Chen, A. M. Kolpak, and S. Ismail-Beigi, Adv. Mater. **22**, 2881 (2010).

[6] S. Stemmer and S. J. Allen, Annu. Rev. Mater. Res. **44**, 151 (2014).

[7] I. V. Maznichenko, S. Ostanin, A. Ernst, J. Henk, and I. Mertig, Phys. Status Solidi (B) **257**, 1900540 (2020).

[8] J. Goniakowski, F. Finocchi, and C. Noguera, Rep. Prog. Phys. **71**, 016501 (2008).

[9] C. Noguera and J. Goniakowski, Chem. Rev. **113**, 4073 (2013).

[10] N. C. Bristowe, P. Ghosez, P. B. Littlewood, and E. Artacho, J. Phys.: Condens. Matter **26**, 143201 (2014).

[11] C. Nougera and J. Goniakowski, *Oxide Materials at the Two-Dimensional Limit* (Springer, New York, 2016), Vol. 234, Chap. Electrostatics and polarity in 2D Oxides, p. 201.

[12] S. Zeng, W. Lü, Z. Huang, Z. Liu, K. Han, K. Gopinadhan, C. Li, R. Guo, W. Zhou, H. H. Ma *et al.*, ACS Nano **10**, 4532 (2016).

[13] N. Pavlenko, T. Kopp, E. Y. Tsymbal, J. Mannhart, and G. A. Sawatzky, Phys. Rev. B **86**, 064431 (2012).

[14] V. Vonk, J. Huijben, D. Kukuruznyak, A. Stierle, H. Hilgenkamp, A. Brinkman, and S. Harkema, Phys. Rev. B **85**, 045401 (2012).

[15] I. V. Maznichenko, S. Ostanin, V. K. Dugaev, I. Mertig, and A. Ernst, Phys. Rev. Materials **2**, 074003 (2018).

[16] I. V. Maznichenko, S. Ostanin, A. Ernst, and I. Mertig, Phys. Rev. Materials **3**, 074006 (2019).

[17] F. Zhang, P. Lv, Y. Zhang, S. Huang, C.-M. Wong, H.-M. Yau, X. Chen, Z. Wen, X. Jiang, C. Zeng, J. Hong, and J. Y. Dai, Phys. Rev. Lett. **122**, 257601 (2019).

[18] Z. Gao, X. Huang, P. Li, L. Wang, L. Wei, W. Zhang, and H. Guo, Adv. Mater. Interfaces **5**, 1701565 (2018).

[19] J. Ye, S. Inoue, K. Kobayashi, Y. Kasahara, H. Yuan, H. Shimotani, and Y. Iwasa, Nat. Mater. **9**, 125 (2010).

[20] S. W. Zeng, X. M. Yin, T. S. Herng, K. Han, Z. Huang, L. C. Zhang, C. J. Li, W. X. Zhou, D. Y. Wan, P. Yang, J. Ding, A. T. S. Wee, J. M. D. Coey, T. Venkatesan, A. Rusydi, and A. Ariando, Phys. Rev. Lett. **121**, 146802 (2018).

[21] E. Maniv, Y. Dagan, and M. Goldstein, MRS Adv. **2**, 1243 (2017).

[22] I. Pallecchi, F. Telesio, D. Li, A. Fête, S. Gariglio, J.-M. Triscone, A. Filippetti, P. Delugas, V. Fiorentini, and D. Marré, Nat. Commun. **6**, 6678 (2015).

[23] P. Gallagher, M. Lee, T. A. Petach, S. W. Stanwyck, J. R. Williams, K. Watanabe, T. Taniguchi, and D. Goldhaber-Gordon, Nat. Commun. **6**, 6437 (2015).

[24] W. Liu, S. Gariglio, A. Fête, D. Li, M. Boselli, D. Stornaiuolo, and J.-M. Triscone, APL Mater. **3**, 062805 (2015).

[25] P. Xu, W. Han, P. M. Rice, J. Jeong, M. G. Samant, K. Mohseni, H. L. Meyerheim, S. Ostanin, I. V. Maznichenko, I. Mertig *et al.*, Adv. Mater. **29**, 1604447 (2017).

[26] M. Sumets, *Lithium Niobate-Based Heterostructures* (IOP, Bristol, England, 2018), pp. 2053–2563.

[27] G. Herranz, F. Sánchez, N. Dix, M. Scigaj, and J. Fontcuberta, Sci. Rep. **2**, 758 (2012).

[28] S. Davis, V. Chandrasekhar, Z. Huang, K. Han, Ariando, and T. Venkatesan, Phys. Rev. B **95**, 035127 (2017).

[29] P. K. Rout, I. Agireen, E. Maniv, M. Goldstein, and Y. Dagan, Phys. Rev. B **95**, 241107(R) (2017).

[30] U. Khanna, P. K. Rout, M. Mograbi, G. Tuvia, I. Leermakers, U. Zeitler, Y. Dagan, and M. Goldstein, Phys. Rev. Lett. **123**, 036805 (2019).

[31] Y. A. Bychkov and É. I. Rashba, Pisma Zh. Eksp. Teor. Fiz. **39**, 66 (1984) [JETP Lett. **39**, 78 (1984)].

[32] A. D. Caviglia, M. Gabay, S. Gariglio, N. Reyren, C. Cancellieri, and J.-M. Triscone, Phys. Rev. Lett. **104**, 126803 (2010).

[33] H. Mirhosseini, I. V. Maznichenko, S. Abdelouahed, S. Ostanin, A. Ernst, I. Mertig, and J. Henk, Phys. Rev. B **81**, 073406 (2010).

[34] P. Noël, F. Trier, L. M. V. Arche, J. Bréhin, D. C. Vaz, V. Garcia, S. Fusil, A. Barthélémy, L. Vila, M. Bibes *et al.*, Nature **580**, 483 (2020).

[35] V. M. Edelstein, Solid State Commun. **73**, 233 (1990).

[36] K. Kondou, R. Yoshimi, A. Tsukazaki, Y. Fukuma, J. Matsuno, K. Takahashi, M. Kawasaki, Y. Tokura, and Y. Otani, Nat. Phys. **12**, 1027 (2016).

[37] A. Brinkman, M. Huijben, M. van Zalk, J. Huijben, U. Zeitler, J. C. Maan, W. G. van der Wiel, G. Rijnders, D. H. A. Blank, and H. Hilgenkamp, Nat. Mater. **6**, 493 (2007).

[38] D. Doennig and R. Pentcheva, Sci. Rep. **5**, 7909 (2015).

[39] J. M. D. Coey, M. Venkatesan, and P. Stamenov, J. Phys.: Condens. Matter **28**, 485001 (2016).

[40] D.-S. Park, A. D. Rata, I. Maznichenko, S. Ostanin, Y. L. Gan, S. Agrestini, G. Rees, M. Walker, J. Li, J. Herrero-Martin *et al.*, Nat. Commun. **11**, 3650 (2020).

[41] G. Kresse and J. Furthmüller, Phys. Rev. B **54**, 11169 (1996).

[42] J. P. Perdew, K. Burke, and M. Ernzerhof, Phys. Rev. Lett. **77**, 3865 (1996).

[43] H. L. Meyerheim, F. Klimenta, A. Ernst, K. Mohseni, S. Ostanin, M. Fechner, S. Parihar, I. V. Maznichenko, I. Mertig, and J. Kirschner, Phys. Rev. Lett. **106**, 087203 (2011).

[44] R. Guo, L. Tao, M. Li, Z. Liu, W. Lin, G. Zhou, X. Chen, L. Liu, X. Yan, H. Tian *et al.*, Sci. Adv. **7**, eabf1033 (2021).

[45] D. Hobbs, G. Kresse, and J. Hafner, Phys. Rev. B **62**, 11556 (2000).

[46] B. Gao, R. Jalem, and Y. Tateyama, ACS Appl. Mater. Interfaces **13**, 11765 (2021).

[47] V. Borisov, S. Ostanin, and I. Mertig, Phys. Chem. Chem. Phys. **17**, 12812 (2015).

[48] K. D. Fredrickson and A. A. Demkov, Phys. Rev. B **91**, 115126 (2015).

[49] U. Herath, P. Tavadze, X. He, E. Bousquet, S. Singh, F. Muñoz, and A. H. Romero, Comput. Phys. Commun. **251**, 107080 (2020).

[50] L. Tao and E. Y. Tsymbal, npj Comput. Mater. **6**, 172 (2020).

[51] Y. Feng, Q. Jiang, B. Feng, M. Yang, T. Xu, W. Liu, X. Yang, M. Arita, E. F. Schwier, K. Shimada *et al.*, Nat. Commun. **10**, 4765 (2019).

[52] D. C. Vaz, P. Noël, A. Johansson, B. Göbel, F. Y. Bruno, G. Singh, S. Mckeown-Walker, F. Trier, L. M. Vicente-Arche, A. Sander *et al.*, Nat. Mater. **18**, 1187 (2019).

[53] M. Basletic, J.-L. Maurice, C. Carrétéro, G. Herranz, O. Copie, M. Bibes, É. Jacquet, K. Bouzehouane, S. Fusil, and A. Barthélémy, Nat. Mater. **7**, 621 (2008).